FLOW STRESS NUMERICAL MODELING FOR LARGE STRAIN DEFORMATION IN MAGNESIUM ALLOY AZ31

LUIGI DE PARI JR[1], WOJCIECH Z. MISIOLEK[1]*, JOY H. FORSMARK[2], ALAN A. LUO[3]

[1] *Institute for Metal Forming, Lehigh University, Bethlehem, PA, USA*
[2] *Ford Motor Company, Research and Innovation Center, Dearborn, MI, USA*
[3] *General Motors Research and Development Center, Warren, MI, USA*
*Corresponding Author: wzm2@lehigh.edu

Abstract

An existing flow stress model proposed by Barnett was examined with as-cast homogenized AZ31 compression test data for a range of temperatures (250-450°C) and strain rates (0.001-20s^{-1}) from literature to verify the applicability of the model to direct extrusion of AZ31. The model was successful in predicting the hardening region of the flow curve but was unable to simulate the sizable softening component of the flow curve that as-cast homogenized magnesium alloys tend to have before failure. In order to correct this shortcoming, an empirical softening expression was developed with the same range of temperatures and strain rates. This modified flow stress model was then implemented into the finite element software package DEFORMTM 3-D to examine the hot-direct extrusion of hollow AZ31 automobile structural components fabricated using a port-hole die.

Key words: magnesium alloys, thermo-mechanical processing, extrusion, recovery, flow stress, numerical simulation

1. INTRODUCTION

There is a growing need to develop fabrication technologies for lightweight components for automotive structural applications. A leading material candidate for such applications is magnesium (Mg) and its alloys due to their attractive physical properties: approximately two-thirds the density of aluminum, high specific strength, good weldability (under a controlled atmosphere), and good damping capacity. The low density of magnesium alloys (1.74 g/cm^3) makes them attractive for structural automotive applications because of the potential of improving fuel efficiency and vehicle performance through reducing vehicle weight while increasing the ability to meet new legislation limiting automobile emissions.

The use of magnesium alloys has been mainly hindered by its low elastic modulus, limited cold workability and toughness, and susceptibility to corrosion (Srivatsan et al., 1995). Formability and ductility limitations at low temperatures are largely a result of the hexagonal close packed (HCP) crystal structure's tendency to deform through twinning rather than slipping due to the lack of five independent slip systems (Srivatsan et al., 1995; Tadano et al., 2007; Wonsiewicz & Backofen, 1967) required for homogeneous plastic deformation as defined by the von Mises criterion (von Mises, 1928). Slip can occur at room temperature along the (0001) basal planes in slip directions perpendicular to the c-axis of the crystal, but this does not allow for extension or contraction of the c-axis. In order to accommodate a shape change in the hexagonal crystal, magnesium alloys tend to twin on $\{10\bar{1}2\}$ planes to

extend the c-axis, or twin on the $\{10\bar{1}1\}$ planes followed by retwinning on the $\{10\bar{1}2\}$ planes to contract the c-axis (Wonsiewicz & Backofen, 1967). These two types of twinning can be referred to as "tension" and "contraction" twinning, respectively (Barnett, 2007a; Barnett, 2007b).

Mg alloy formability can be improved at elevated temperatures through the activation of additional slip systems (such as prismatic $\{10\bar{1}0\}\langle1\bar{2}10\rangle$, pyramidal $\{1\bar{1}01\}\langle11\bar{2}0\rangle$, and <c+a> $\{1\bar{2}12\}\langle1\bar{2}1\bar{3}\rangle$ (Levesque et al., 2006; Levesque et al., 2007) despite increases in production costs. This leads to the need for better understanding of Mg alloy deformation at elevated temperatures and, specifically, the flow stress behavior at elevated temperatures so that processing improvements can potentially be developed for industrial magnesium extrusions.

The approach taken in this study was to link the state variables, strain, strain rate, and temperature to the prediction of flow stress during extrusion of as-cast homogenized magnesium alloy AZ31. The reason for this is to have a numerical model that is capable of predicting the sophisticated flow stress response but also can easily be used within an industry-accepted software package such as LS-DYNA, DEFORM, QFORM, and others. This allows the suppliers of the extruded components to test the extrusion feasibility with a higher a degree of accuracy without requiring the suppliers to have a high level of theoretical understanding of microstructural phenomena and crystal plasticity as required by many existing scientific models (Agnew & Duygulu, 2005; Lebensohn & Tome, 1993; Levesque et al., 2006; Levesque et al., 2007; Staroselsky & Anand, 1998; Staroselsky & Anand, 2003; Tadano et al., 2007; Van Houtte, 2001). Moreover, this will minimize the timely and costly exploratory extrusion trials done by industry, as well as, minimize the effort to determine the extensive series of single-crystal parameters and material-specific curve fitting constants done by the scientific researchers. The single-crystal parameters are often determined through iteration and describe the evolution of the critical resolved shear stress for each of the twinning and slip modes (Barnett et al., 2005; Staroselsky & Anand, 1998). Material-specific curve fitting constants generally require assessing certain measurements from a specific material orientation. The scientific models, though, can predict the macro-scale

stress response (Francillette et al., 2003; Levesque et al., 2006; Tadano et al., 2007) in addition to the micro-scale texture evolution (Levesque et al., 2006; Tadano et al., 2007), twin initiation (Meyers et al., 2001) and the influence of twin boundaries on slip (Remy, 1978); features a simpler model would have difficulty performing reliably.

Models of less complexity have been developed (Li et al., 2006; Mathis et al., 2002; Mathis et al., 2004; Sheng & Shivpuri, 2006; Slooff et al., 2007; Takuda et al., 2005) but they are inappropriate to reproduce the entire flow stress curve for the wide range of strain, strain rate, and temperature conditions that occur during a typical deformation processing such as extrusion. The reason for this is the equations chosen to govern some models only predict the hardening component of the flow curve; for instance the Hollomon equation: $\sigma = K\varepsilon^n$. This only allows the models to be valid up to a small level of plastic strain (e.g. 0.2) (Barnett et al., 2006; Barnett et al., 2005). Such a limitation would make the flow stress model inappropriate for the simulation of extrusion where the strain levels can easily climb to values of 8 or 9 or even higher depending on the forming conditions.

Additionally, many of the less complex models are not constructed as functions of all three state variables, strain, ε, strain rate, $\dot{\varepsilon}$, and temperature, T but rather only functions of one or two of the state variables. Examples include the Hollomon equation, which is only a function of the state variable ε, or the following equation, which is only a function of the state variables $\dot{\varepsilon}$ and T:

$$\sigma = \frac{1}{\alpha}\left\{\left(\frac{Z}{A}\right)^{1/n} + \left[\left(\frac{Z}{A}\right)^{2/n} + 1\right]^{1/2}\right\} = f(\dot{\varepsilon}, T) \quad (1)$$

where the Zener-Hollomon parameter, $Z = \dot{\varepsilon}\exp(Q/RT)$, is a temperature-modified strain rate term. Equation (1) is derived from the more familiar relationship

$$\dot{\varepsilon} = A[\sinh(\alpha\sigma)]^n \exp\left(\frac{-Q}{RT}\right) \quad (2)$$

Few models exist between the scientific type models and models of less complexity. Barnett et al. (2006) developed such a flow stress model that offered a balance in required material data and mathematic intricacy. Based on the dominance of basal slip and $\{10\bar{1}2\}$ twinning during plastic deforma-

tion a semianalytical description for flow stress was developed to capture these two separate effects in Mg alloys. The model is a based on average Schmid factors for basal slip and $\{10\bar{1}2\}$ twinning, the rate of twinning, and the relative values of the critical resolved shear stresses (CRSSs). Using an effective Schmid factor to quantify the effect of different portions of the polycrystalline sample as opposed to using the specific Schmid factor for each crystal and then relating them back to each other with iterative polycrystalline equations as required by the scientific (or self-consistent) models, simplifies the required mathematics significantly. The model proposed by Barnett et al. (2006) is unhindered by iteration through strain; allowing it to provide rapid solutions in an explicit manner. The key assumption made in this model is the Sachs assumption; that only one slip or twinning system is considered to operate in each grain at a time (Barnett et al., 2006; Hosford, 1993). Since only a limited number of systems are available to accommodate deformation within a grain during any given loading condition (basal slip only provides two independent systems for shear which typically takes place in either sense along a slip direction on a slip plane, while $\{10\bar{1}2\}$ twinning only provides six independent systems for shear that typically take place in a single sense (Barnett et al. 2006; Barnett et al. 2005; Staroselsky & Anand, 2003), the Sachs assumption is a reasonable one.

The governing equation for the model is presented below:

$$\sigma = (1-\chi)X_T\frac{\tau_{0t}}{m_I} + \chi X_T \xi \frac{k}{m_{II}^{n+1}}(\varepsilon - 0.13m_I\chi)^n +$$
$$(1-X_T)\frac{k}{m_{III}^{n+1}}\varepsilon^n \qquad (3)$$

Equation (3) is comprised of three terms that separate the Mg alloy grains into three different volumes. Volume I, defined as $(1-\chi)X_T$, is the material that deforms by twinning where X_T is the fraction of grains undergoing twinning and χ is the fraction of these grains that have twinned. Volume II, defined by χX_T, is the material that has twinned but subsequently deforms by slip. Volume III, defined by $(1-X_T)$, is the material that deforms only by slip.

The stress in volume I, σ_I, is defined in equation (4) (or Schmid's Law) and is represented in the first term of equation (3). Here m_I is the effective Schmid factor and τ_{0t} is the CRSS for twinning for this vol-

ume (Barnett et al., 2006). It is assumed that this stress does not change with strain because of the "easy" advancement of the $\{10\bar{1}2\}$ twinning front once the twin has formed (Barnett et al., 2006).

$$\sigma_I = \frac{\tau_{0t}}{m_I} \qquad (4)$$

The stress in volume II, σ_{II}, is defined in equation (5) and represented in the second term of equation (3). Here m_{II} is the effective Schmid factor and k reflects the magnitude of the CRSS for basal slip after twinning for this volume (Barnett et al., 2006).

$$\sigma_{II} = \xi\frac{k}{m_{II}^{n+1}}(\varepsilon - 0.13m_I\chi)^n \qquad (5)$$

where ε is strain, n is a constant, and ξ is a curve-fitting hardening factor added by Barnett et al. (2006) to introduce additional hardening. The stress in volume III, σ_{III}, is defined in equation (6) and represented in the third term of equation (3). Here m_{III} is the effective Schmid factor for basal slip for this volume, which does not undergo twinning (Barnett et al., 2006).

$$\sigma_{III} = \frac{k}{m_{III}^{n+1}}\varepsilon^n \qquad (6)$$

The value of χ is controlled by the sigmoidal relationship of equation (7), which agrees with experimental observations (Jiang et al., 2007a). The variable a is a rate exponent and ε_I is the macroscopic strain where the twinning reaction has reached 98% completion.

$$\chi = 1 - \exp\left[-4\left(\frac{\varepsilon}{\varepsilon_1}\right)^a\right] \qquad (7)$$

The Barnett et al. (2006) flow stress model was examined with the AZ31 as-cast homogenized compression test data for a range of temperatures (250-450°C) and strain rates (0.001-20 s^{-1}) from literature to verify the applicability of the model to AZ31 direct extrusion. The model was successful in predicting the hardening component of the flow curve for low strain but was unable to simulate the sizable recovery component of the flow curve that as-cast homogenized Mg alloys tend to have before failure due to the fact that it is only a hardening model. Predicting only the hardening component of the stress-strain curve is a common characteristic among the majority of the models that are currently in lit-

erature; scientific or simplified. In order to correct for this shortcoming, an empirical softening expression was developed for the model with the same range of temperatures and strain rates.

2. MODEL DESCRIPTION

The limitation of the Barnett et al. (2006) flow stress model is that it only accounts for the hardening behavior of the true (stress-strain) flow curve or curve-A of figure 1 (Gronostajski, 2000). The typical softening behavior of an as-cast homogenized Mg alloy at elevated strain levels is represented by curve-B of figure 1 (Gronostajski, 2000; Jiang et al., 2007a; Sheng & Shivpuri, 2006), which comprises hardening, softening, and steady-state. The hardening component of curve-B is represented by a strain of zero to ε_{us}, or the strain at ultimate strength. Some of the mechanisms controlling hardening are the rate of dislocation generation and accumulation, as well as the availability of slip and twinning systems. Material softening, as a result of dynamic recovery, recrystallization, deformation heating, and texture formation, is represented on curve-B from ε_{us} to ε_{ss}, or the strain at the saturation stress. The point of inflexion, ε_{inflex} divides both ε_{us} and ε_{ss}. In order to mimic this softening, an additional term was developed and added to the end of equation (3) as presented on the second line in equation (8). The major benefit with this approach is that there is a single equation predicting the true flow curve unlike with other models that distinguish the three specific ranges in the true flow-curve with three different specific equations of a piecewise function (Gronostajski, 2000; Schindler et al., 1996).
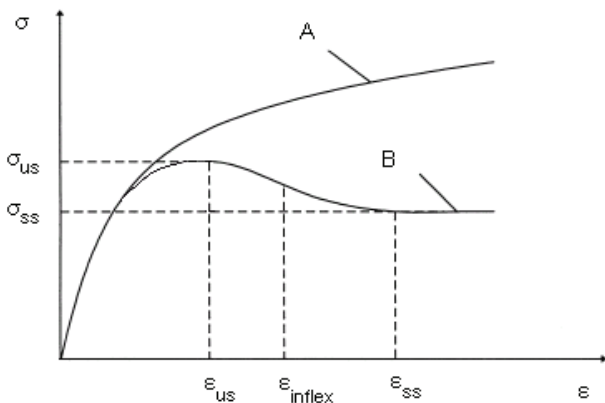
Fig. 1. *True stress-strain behavior as a dependence on material; curve-A is typical of aluminum alloys and curve-B is typical of as-cast homogenized magnesium alloys.*

$$\sigma = (1-\chi)X_T \frac{\tau_{0t}}{m_I} +$$

$$\chi X_T \xi \frac{k}{m_{II}^{n+1}}(\varepsilon - 0.13m_I\chi)^n + (1-X_T)\frac{k}{m_{III}^{n+1}}\varepsilon^n$$

$$+\left[A(\exp(-B\varepsilon)-1)+C(\exp(-20\varepsilon)-1)\varepsilon^D\right] \quad (8)$$

The softening term is an empirical relationship, with each of the four variables generally controlling a specific feature of the softening component of the flow curve. Variable A has the largest impact on the slope of the curve between ε_{us} and ε_{inflex}. As *A* increases the magnitude of the negative slope increases. Additionally, the majority of the flow curve can decrease. Variable *B* has the largest impact on controlling the value of the ultimate strength, σ_{us}. As *B* increases σ_{us} decreases with the majority of the flow curve shifting downward. The slope of the curve between ε_{inflex} and ε_{ss} is controlled by variable *C*. As *C* increases the magnitude of the negative slope in this range increases with the majority of the tail-end of the flow curve moving downward. The variable *D* impacts the tail-end of the flow curve which starts at ε_{ss} or the beginning of the steady-state region. As *D* increases the magnitude of the negative slope in this range increases with the majority of the other features of the flow curve remaining unchanged.

Another change to equation (3) was to redefine *k* in the second and third term. Originally, *k* was defined as reflecting the magnitude of the CRSS for basal slip after twinning. Here *k* will be defined as in equation (9), where *K* is the strength coefficient of the Hollomon relationship.

$$k = \frac{K}{10} \quad (9)$$

A log-log plot of true stress and true strain up to the maximum load, σ_{us} will result in approximately a straight line. The slope of this line is *n*, the strain-hardening exponent, and *K* is the true stress at $\varepsilon = 1.0$. The variable *n* in equation (3) was also redefined to the strain-hardening exponent, *n* in the Hollomon relationship. The purpose of redefining the two variables was to experimentally back the values used for *k* and *n* of equation (8). Additionally, the second and third terms of equation (8) are in a form that generally can be described with the Hollomon relationship.

Many of the variables in equation (8) and equation (7) were determined as functions of strain rate and temperature through curve fitting but values for some variables, such as X_T and ε_I, were kept close to previously seen experimental values. By quantifying the variables in this way the model now becomes a function of ε, $\dot{\varepsilon}$, and T, that reasonably meets experimental expectations for the variables. Curve fitting will produce values for the variables but if the data set is small the variable values are usually only suitable within a small range of the originally considered data set. In order to minimize this limitation, a sizable amount of AZ31 as-cast homogenized compression true flow stress data at extrusion suitable temperatures and strain rates was identified from the literature (Barnett et al., 2004; Beer & Barnett, 2007; Guo et al., 2006; Lapovok et al., 2004; Wang et al., 2007) and used to determine the relationships for the variables in equation (8) and equation (7). The specific strain rates and temperatures considered are described in table 1.

Table 1. *Temperatures and strain rates for AZ31 as-cast homogenized flow stress data.*

Temperature (^{o}C)	Strain Rates (s^{-1})
250	0.03, 0.3, 3
300	0.005, 0.05
350	0.01, 0.1
400	0.03, 0.1, 0.3, 3
450	0.001, 0.01, 0.1, 1, 10, 20

A program was written with MATLAB^{TM} to digitize the literature flow stress curve images that allowed the extraction of the stress-strain data points at a suitable strain step-size to accurately reproduce the flow stress curve. In general, at least 100 data point sets were extracted from each curve with two examples of the extracted curves shown in figure 2.

The purpose for only using as-cast homogenized Mg alloy flow stress data is that during extrusion of automotive structural components the as-cast billet is generally deformed once to a slightly smaller diameter for homogenization purposes and then extruded a second time into the final shape. Once a Mg alloy is plastically deformed into its final shape it tends to develop a very strong textured grain orientation that significantly influences the true stress-strain behavior of the Mg alloy (Agnew & Duygulu, 2005; Barnett, 2001; Barnett, 2005; Barnett, 2007a; Barnett, 2007b).

Compression flow stress data was used because the stress-state within hot-direct extrusion is primarily compression and a sufficient amount of flow stress curves at extrusion suitable temperatures and strain rates could be identified from the literature. Shear is the other major stress-state found in the hot-direct extrusion process and occurs near the container wall; within the shear-band that defines the dead-metal zone, and as the material is moving through the die. Torsion testing is a good experimental test to replicate the shear stress, but, a suitable amount of flow stress curves at extrusion suitable temperatures and strain rates could not be identified from the literature.
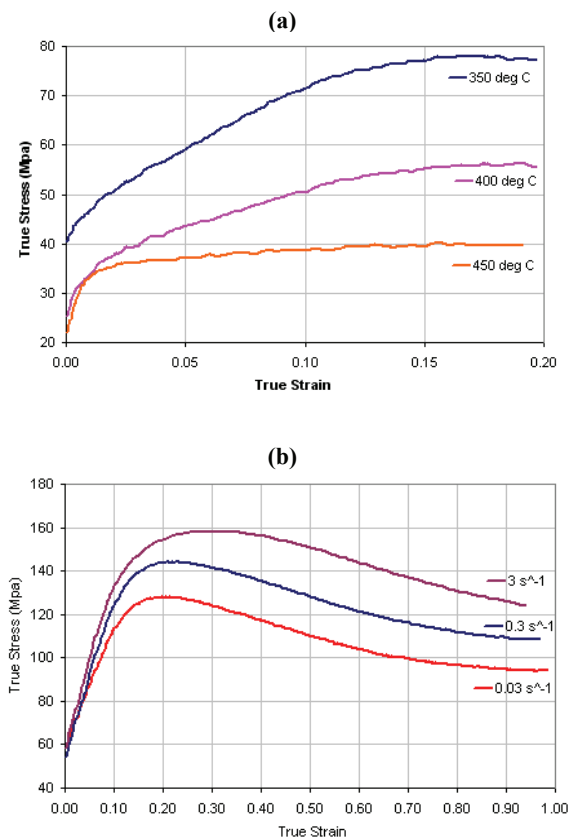
Fig. 2. *AZ31 as-cast homogenized compression true flow stress data. (a) Constant strain rate = 0.1 s^{-1} (Barnett et al., 2004). (b) Constant temperature = 250°C (Lapovok et al., 2004).*

Once the relationships were developed for the variables in equation (8) and equation (7), they were implemented into the finite element software package DEFORM^{TM} 3-D along with equation (7) and equation (8) to examine the hot-direct extrusion of a hollow AZ31 automobile structural component fabricated using a porthole die.

The structural component analyzed in this study is an industrially produced "double hat" typical of a crash-box design (figure 3) used by the automotive industry. The geometry of the extrusion in figure 3 is created with the 8 port-hole die shown in figure 4.
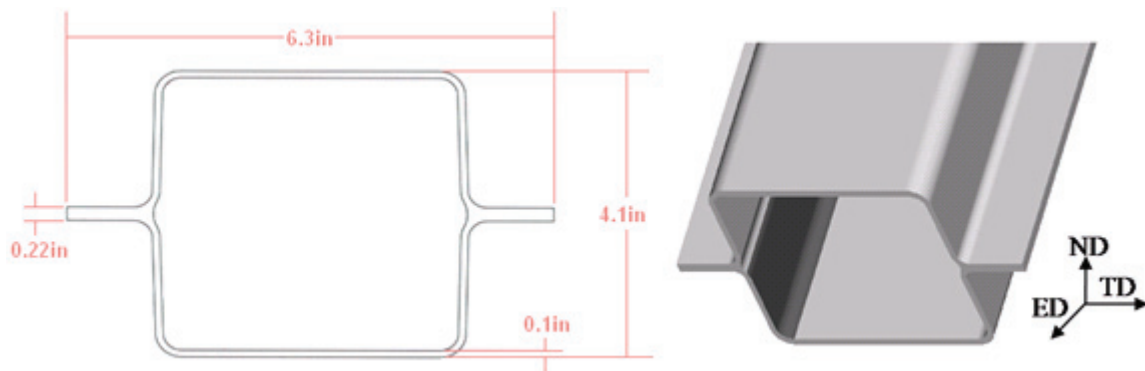
Fig. 3. Double-hat extrudate. ED: Extrusion Direction, ND: Normal Direction, TD: Transverse Direction.
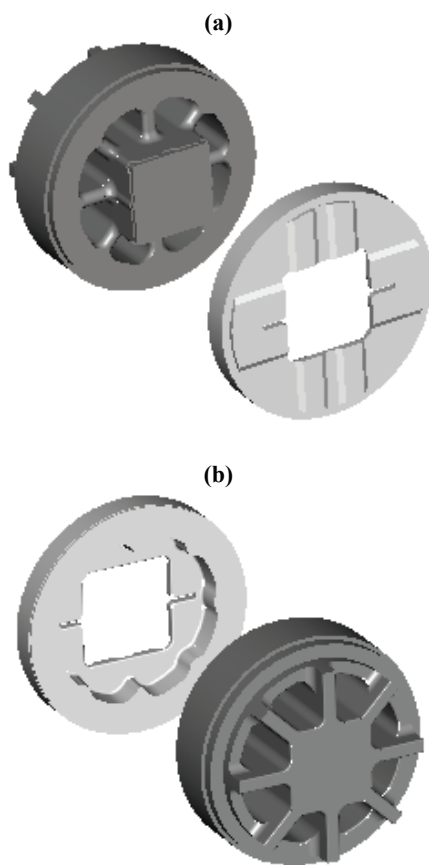

(a)

(b)

Fig. 4. (a) Front- and (b) rear-view of the 8 port-hole die-assembly.

The initial conditions for the DEFORM™ 3-D simulation are listed in table 2. The billet diameter and extrudate dimensions are set to the industrial processing conditions. The billet and tooling temperatures are set to the initial temperatures found in the industrial process before extrusion begins.

The AZ31 billet was modeled as a perfectly-plastic object in all simulations. With an initial temperature of 538ºC (1000ºF), which is 85% - 89% of the 605 - 630°C (1120 - 1170 °F) melting temperature range, any residue elastic behavior would be recovered and not influence the deformation process.

Table 2. Initial conditions for the DEFORM™ 3-D Mg double-hat extrusion.

Billet Diameter x Billet Length	200 mm (7.87 in) x 240 mm (9.45 in)
Billet Temperature	538ºC (1000ºF)
Tooling Temperature	427ºC (800ºF)
Environment (Air) Temperature	20ºC (68ºF)
Shear Friction Coefficient (Billet – Billet)	0.7
Shear Friction Coefficient (Billet – Tooling)	0.2
Ram Speed	1.32 mm/s (0.052 in/s)
Heat Transfer Coefficient (Billet - Billet)	11000 W/(m^2 ºC) (0.538 Btu/(s ft^2 ºF))
Heat Transfer Coefficient (Billet - Tooling)	5000 W/(m^2 ºC) (0.245 Btu/(s ft^2 ºF))
Time Step	0.1 – 0.2 s
Mesh Element Range	1.0 mm – 12 mm (0.04 in – 0.47 in)

The remaining tools (container, 8 port-hole die, and ram) were modeled as rigid objects in all simulations. They are made from tool steel and were either suitably bolstered, or had substantial size that no deformation was assumed to occur.

3. RESULTS

The Mg alloy examined during this study was AZ31 (3 wt% Al, 1 wt% Zn). While AZ31 is the most popular magnesium extrusion alloy, a new alloy, AM30 (3 wt% Al, 0.3 wt% Mn), with improved formability and extrudability is being considered for the automotive structural components. As discussed by Luo & Sachdev (2007), the major difference between the alloys is a decrease in zinc content in alloy AM30. The added strength imparted from zinc additions was sacrificed in the interest of improving ductility and hence extrudability which

leads to reduced production times and cost. table 3 gives typical compositions for both AZ31 and AM30 alloys (Luo & Sachdev, 2007).

Table 3. *Typical chemical compositions (wt%, bal Mg) of AZ31 and AM30 components.*

Alloy	Al	Mn	Zn	Fe	Ni	Cu
AZ31	3.1	0.54	1.05	0.0035	0.0007	0.0008
AM30	3.4	0.33	0.16	0.0026	0.0006	0.0008

An attempt to identify AM30 as-cast homogenized flow stress data at extrusion suitable temperatures and strain rates was undertaken but minimal data could be found in literature (Wang et al., 2007) to verify the validity of the model. Therefore, since both alloys perform similarly in terms of flow stress (Jiang et al., 2007b; Luo & Sachdev, 2007), and since a suitable amount of AZ31 as-cast homogenized compression true flow stress data at extrusion suitable temperatures and strain rates could be found in literature (Barnett et al., 2004; Beer & Barnett, 2007; Guo et al., 2006; Lapovok et al., 2004; Wang et al., 2007), AZ31 was the alloy chosen for the model analysis. It is expected the final form of the model will only have to be changed slightly to reproduce the AM30 flow stress data once it is obtained.

3.1. Analysis of Modified Flow Stress Model

The values for each variable from equation (7) and equation (8) were determined by reproducing the AZ31 true flow stress curves identified from the literature (Barnett et al., 2004; Beer & Barnett, 2007; Guo et al., 2006; Lapovok et al., 2004; Wang et al., 2007) that correlate to the strain rate and temperature combination in table 1. These values are presented in table 4. Repeated strain rates in table 4 indicate that there were several sets of experimental data from literature for that given combination of strain rate and temperature. A comparison between the flow stress model with these variables and the experimental flow stress curves are presented in

Table 4. *The values for each variable that reproduce the AZ31 flow stress curves found in literature at the specified strain rates and temperatures. Repeated strain rates indicate flow stress data from multiple sources.*

Temperature [°C]	450	450	450	450	450	450	450	400	400	400	400	350	350	300	300	250	250	250
Strain Rate [s^{-1}]	0.001	0.01	0.1	0.1	1	10	20	0.03	0.1	0.3	3	0.01	0.1	0.005	0.05	0.03	0.3	3
Variables:																		
a	1	1	1	1	1	1	1	1	1	1	1	1	1	1	1	1	1	1
$\dot{\varepsilon}_1$	0.18	0.18	0.18	0.18	0.18	0.18	0.18	0.18	0.18	0.18	0.18	0.18	0.18	0.18	0.18	0.18	0.18	0.18
K	27	41	47.5	63	82	120	145	67.5	74	98.5	136	73.5	112	89.5	128	225	260	295
k	2.7	4.1	4.75	6.3	8.2	12	14.5	6.75	7.4	9.85	13.6	7.35	11.2	8.95	12.8	22.5	26	29.5
n	0.035	0.089	0.081	0.133	0.160	0.208	0.230	0.097	0.167	0.151	0.192	0.119	0.203	0.084	0.139	0.305	0.327	0.346
ξ	1	2	2	2	2	1	1	1	1	1	1	1	1	1	1	1	1	1
τ_0†	2	2	2	2	2	2	2	6	6	6	6	9.9	9.9	14	14	18	18	18
m_I	0.09	0.09	0.09	0.09	0.09	0.09	0.09	0.13	0.13	0.13	0.13	0.17	0.17	0.21	0.21	0.25	0.25	0.25
m_{II}	0.074	0.074	0.074	0.074	0.074	0.074	0.074	0.077	0.077	0.077	0.077	0.08	0.08	0.083	0.083	0.086	0.086	0.086
m_{III}	0.46	0.46	0.46	0.46	0.46	0.46	0.46	0.4	0.4	0.4	0.4	0.34	0.34	0.28	0.28	0.22	0.22	0.22
X_T	0.73	0.73	0.73	0.73	0.73	0.73	0.73	0.75	0.75	0.75	0.75	0.77	0.77	0.79	0.79	0.81	0.81	0.81
A	4.2	7.5	9	13	26.5	84	158	29	44.5	62	92.5	48	85	69	110	201	235	286
B	6	4.6	4	4.7	3.8	1.65	1.12	2.7	2.05	2.1	2.05	2.15	2	2.05	1.9	1.98	1.8	1.53
C	2.7	11	15	26.5	44.7	84.5	120	14	32.5	36.5	75.5	17.5	59	10	31	206	272	339
D	0.4	0.4	0.4	0.4	0.4	0.4	0.4	0.438	0.438	0.438	0.438	0.475	0.475	0.5125	0.5125	0.55	0.55	0.55
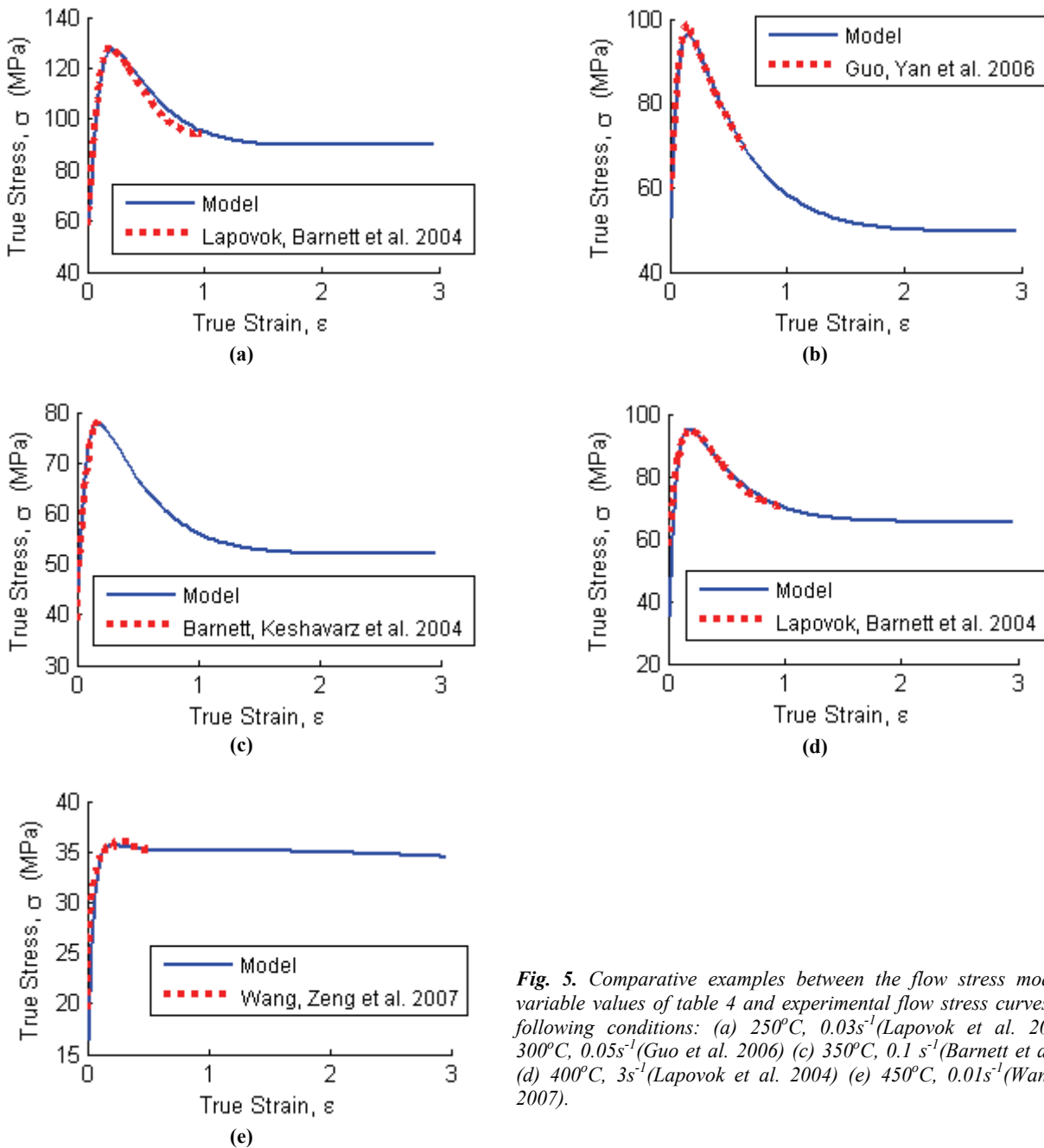
Fig. 5. *Comparative examples between the flow stress model with variable values of table 4 and experimental flow stress curves for the following conditions: (a) 250ºC, 0.03s⁻¹(Lapovok et al. 2004) (b) 300ºC, 0.05s⁻¹(Guo et al. 2006) (c) 350ºC, 0.1 s⁻¹(Barnett et al. 2004) (d) 400ºC, 3s⁻¹(Lapovok et al. 2004) (e) 450ºC, 0.01s⁻¹(Wang et al. 2007).*

When the model variables were plotted with respect to strain rate and temperature, the graphs in figure 6 and figure 7 were produced. Variables a, e_1, and ξ were found to be constant through all strain rates and temperatures with values equal to $a = 1$, $e_1 = 0.18$, and $\xi = 1$.

The graphs in figure 6 and figure 7 that did vary with strain rate (k, n, A, B, and C) are shown in figure 8, figure 9, and figure 10 with tend lines. The trend lines were either of the logarithmic form $(r\ln(\dot{\varepsilon}) + s)$ or the power-law form $(r\dot{\varepsilon}^s)$. This produced relationships for k, n, A, B, and C that were now explicitly a function of strain rate.

The r and s values from the logarithmic and power-law tend lines of figure 8, figure 9, and figure 10 were then plotted with respect to the absolute temperature as presented in figure 11 - figure 15. Trend lines were added. The trend lines were either of the linear form $(pT + q)$, logarithmic form $(p\ln(T) + q)$, exponential form (pe^q) or the power-law form (pT^q). This produced relationships for the r and s values that were now explicitly a function of temperature.

COMPUTER METHODS IN MATERIALS SCIENCE
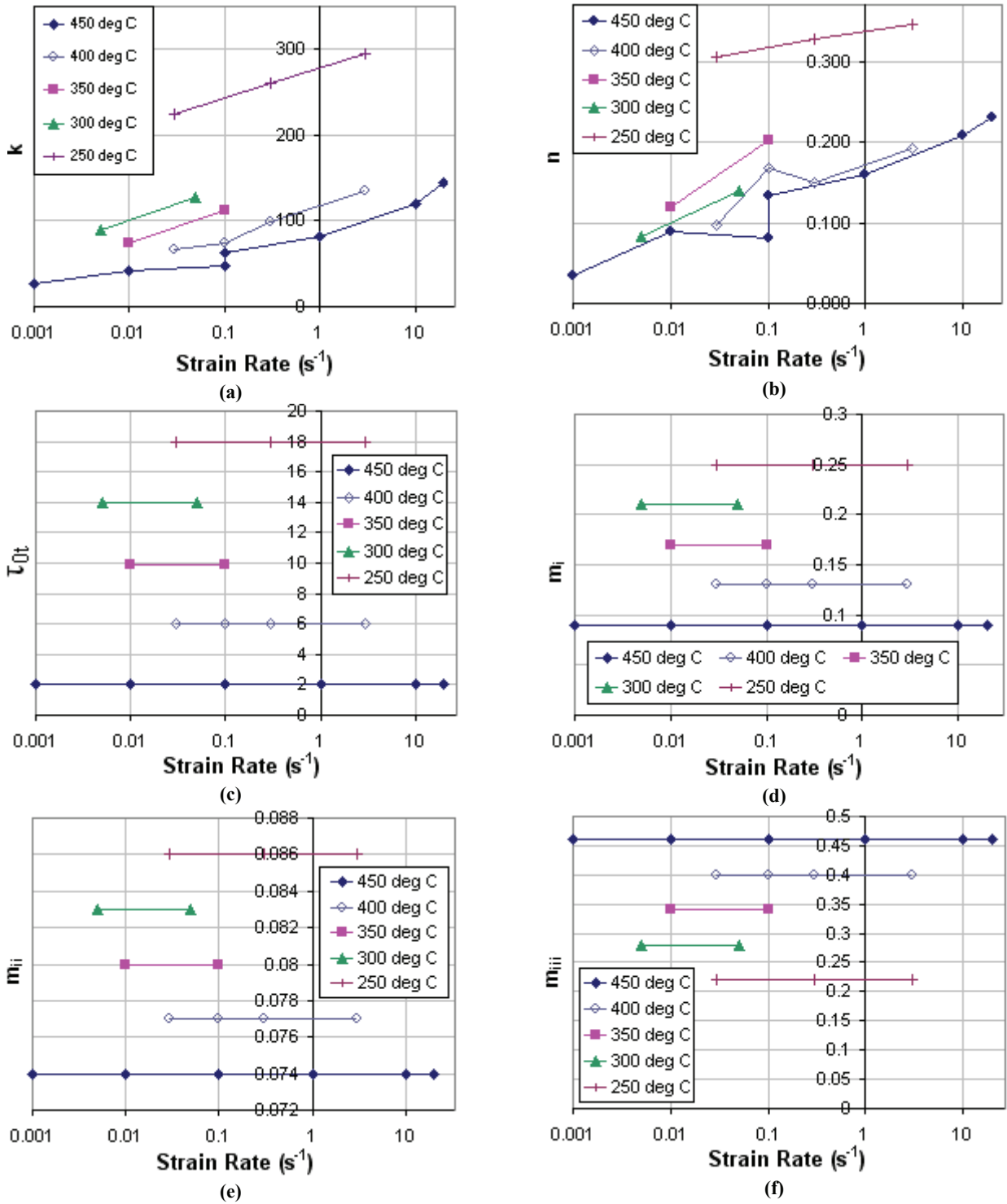
Fig. 6. *A partial set of variables plotted with respect to strain rate and temperature. Variables a, e₁, and ξ are found to be constant through all strain rates and temperatures with the values of a = 1, e₁ = 0.18, and ξ = 1.*
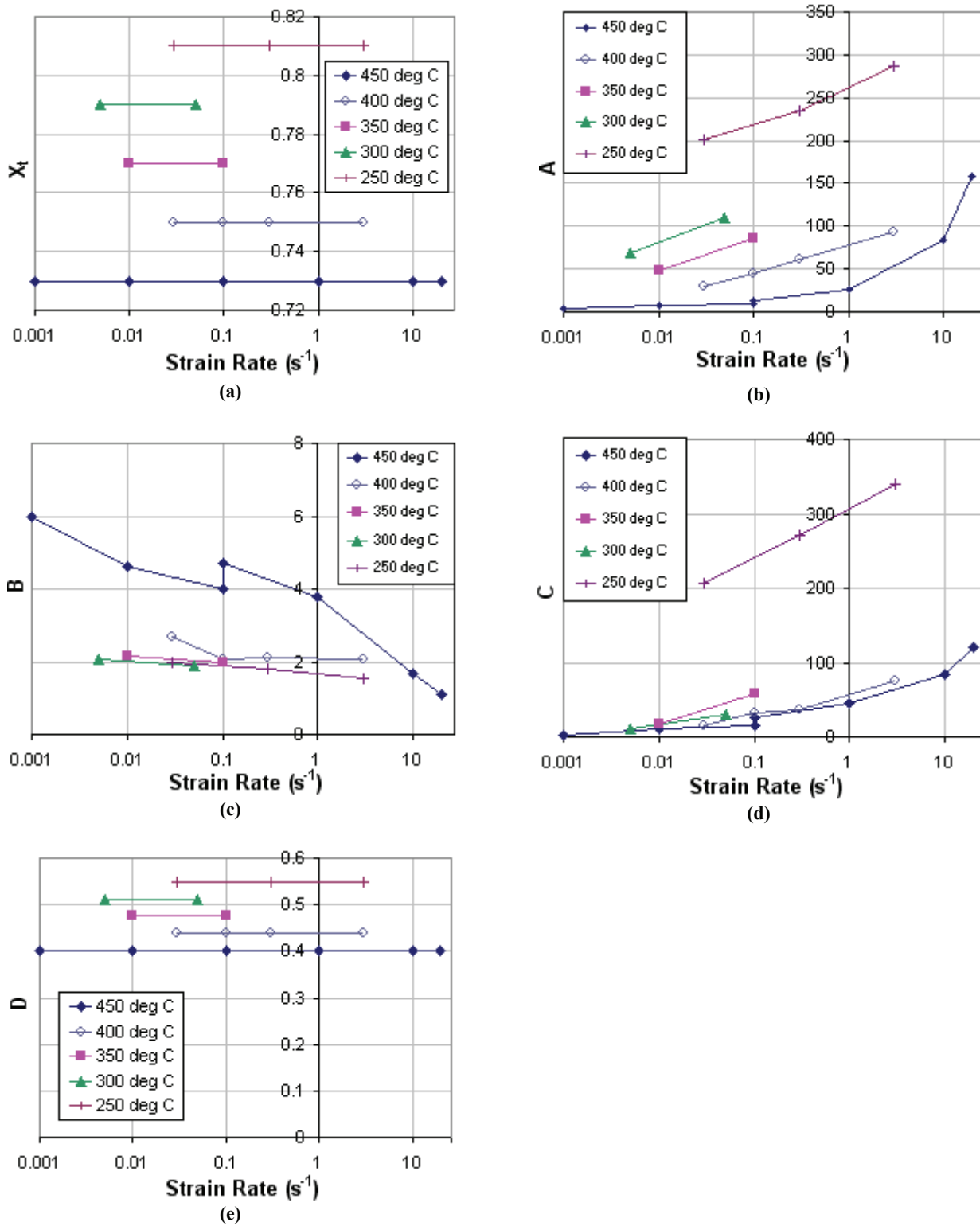
Fig. 7. The remainder of model variables plotted with respect to strain rate and temperature.

(a)

(b)
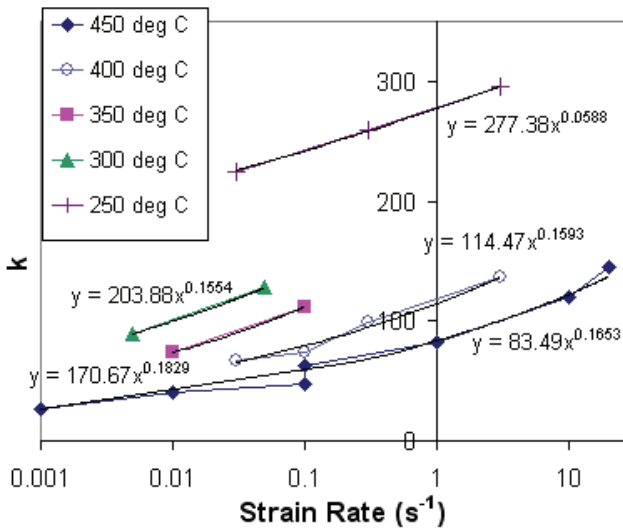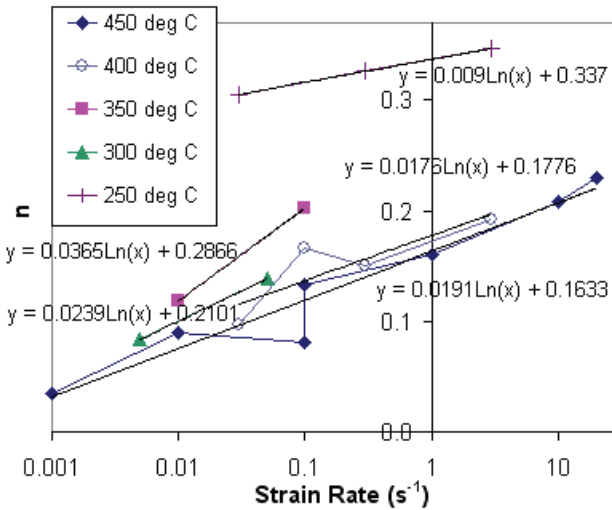
Fig. 8. Tends for variables k and n: k trends with a power-law form $\left(r\dot{\varepsilon}^{s} \right)$ and n trends with a logarithmic form $\left(r\ln(\dot{\varepsilon}) + s \right)$.

Fig. 9. Variable C trends with a power-law form $\left(r\dot{\varepsilon}^{s} \right)$.

(a)

(b)
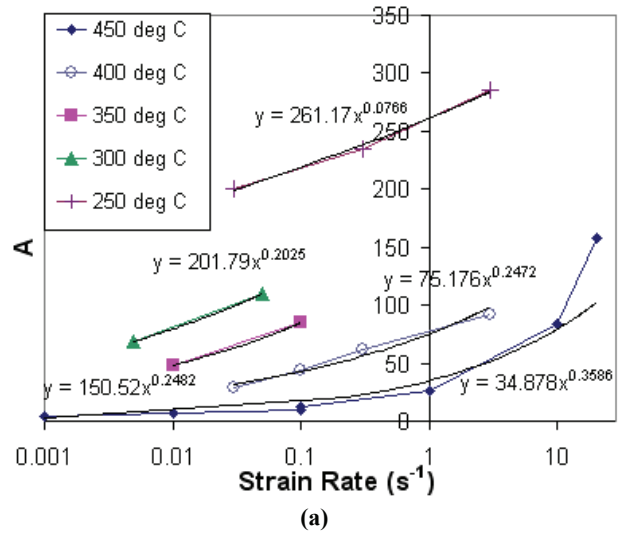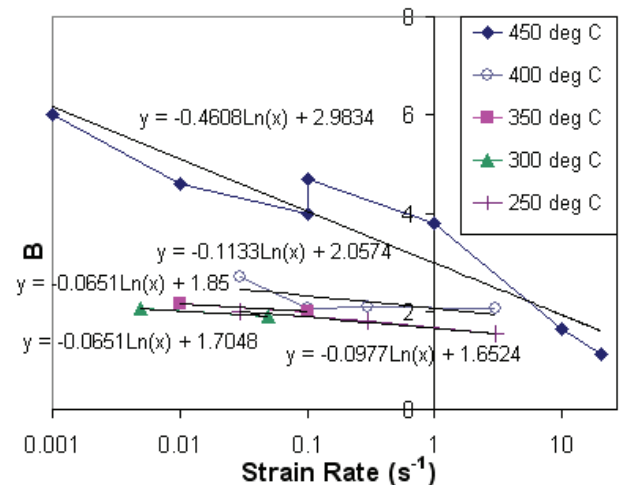
Fig. 10. Tends for variables A and B: A trends with a power-law form $\left(r\dot{\varepsilon}^{s} \right)$ and B trends with a logarithmic form $\left(r\ln(\dot{\varepsilon}) + s \right)$.

The remaining variable graphs in figure 6 and figure 7 did not vary with strain rate (τ_{0t}, m_i, m_{ii}, m_{iii}, X_t, and D) but did vary with temperature. Therefore, these variables were plotted with respect to the absolute temperature in order to develop relationships that were a function of temperature.

The strain rate relationships from figure 8, figure 9, and figure 10 along with the temperature relationships developed in figure 11 - figure 15 were combined to produce relationships for the model variables that were now a function of strain rate and temperature. The new variable functions are presented below in table 5.
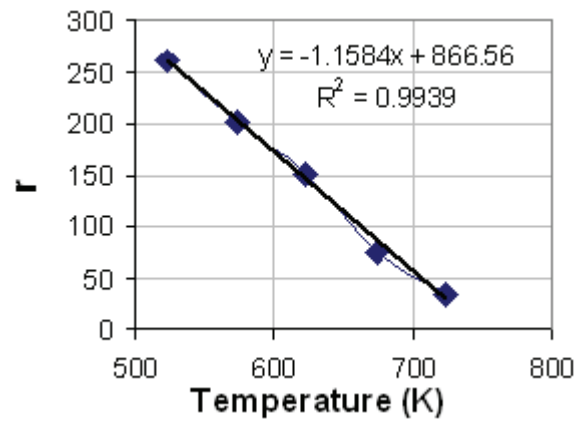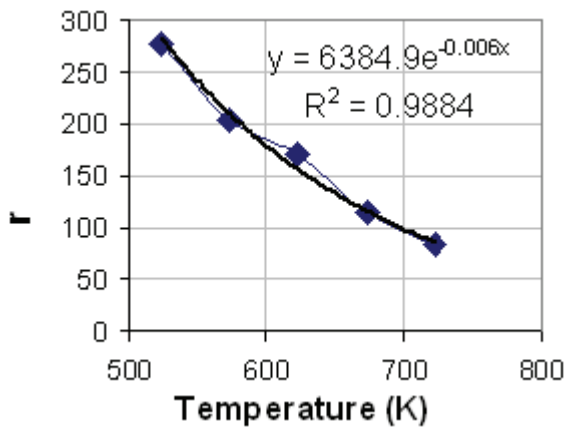
Fig. 11. *The r and s values for variable k from figure 10 are plotted with respect to absolute temperature.*

Fig. 12. *The r and s values for variable n from figure 8 are plotted with respect to absolute temperature.*

Fig. 13. *The r and s values for variable A from figure 9 are plotted with respect to absolute temperature.*
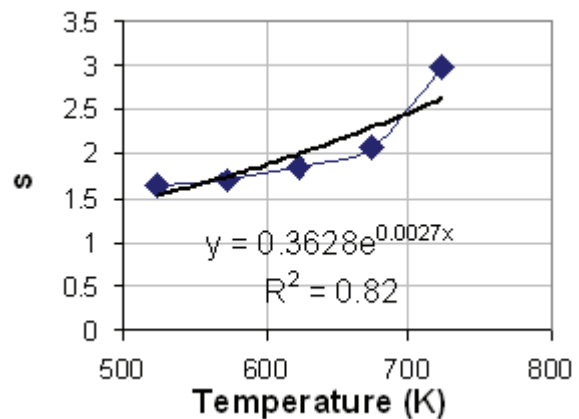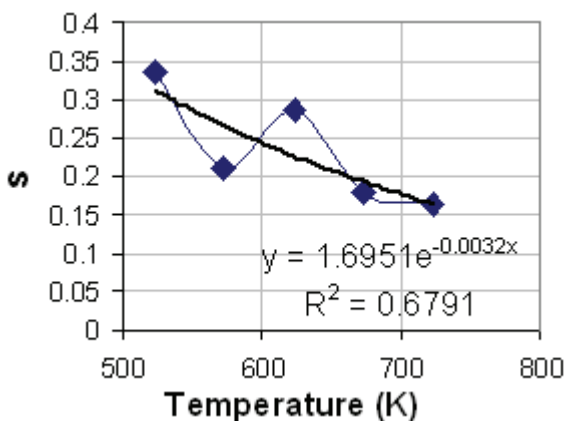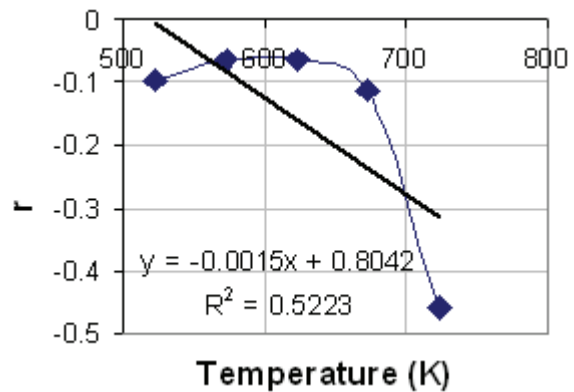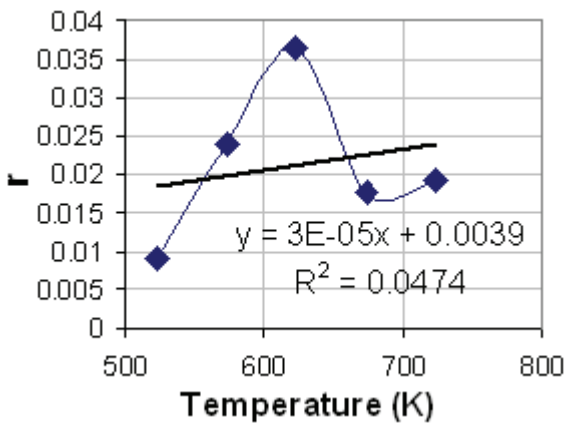

Fig. 14. *The r and s values for variable B from figure 9 are plotted with respect to absolute temperature.*
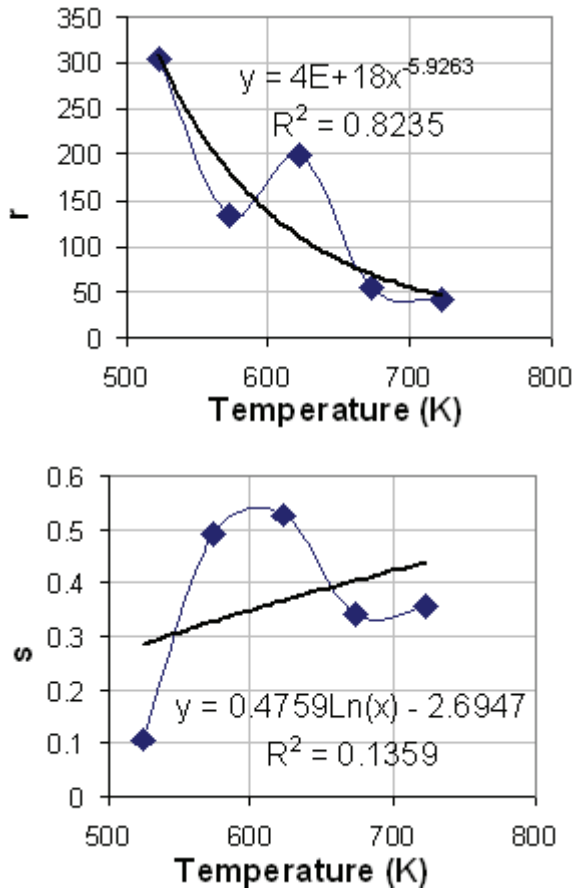
Fig. 15. *The r and s values for variable C from figure 10 are plotted with respect to absolute temperature.*

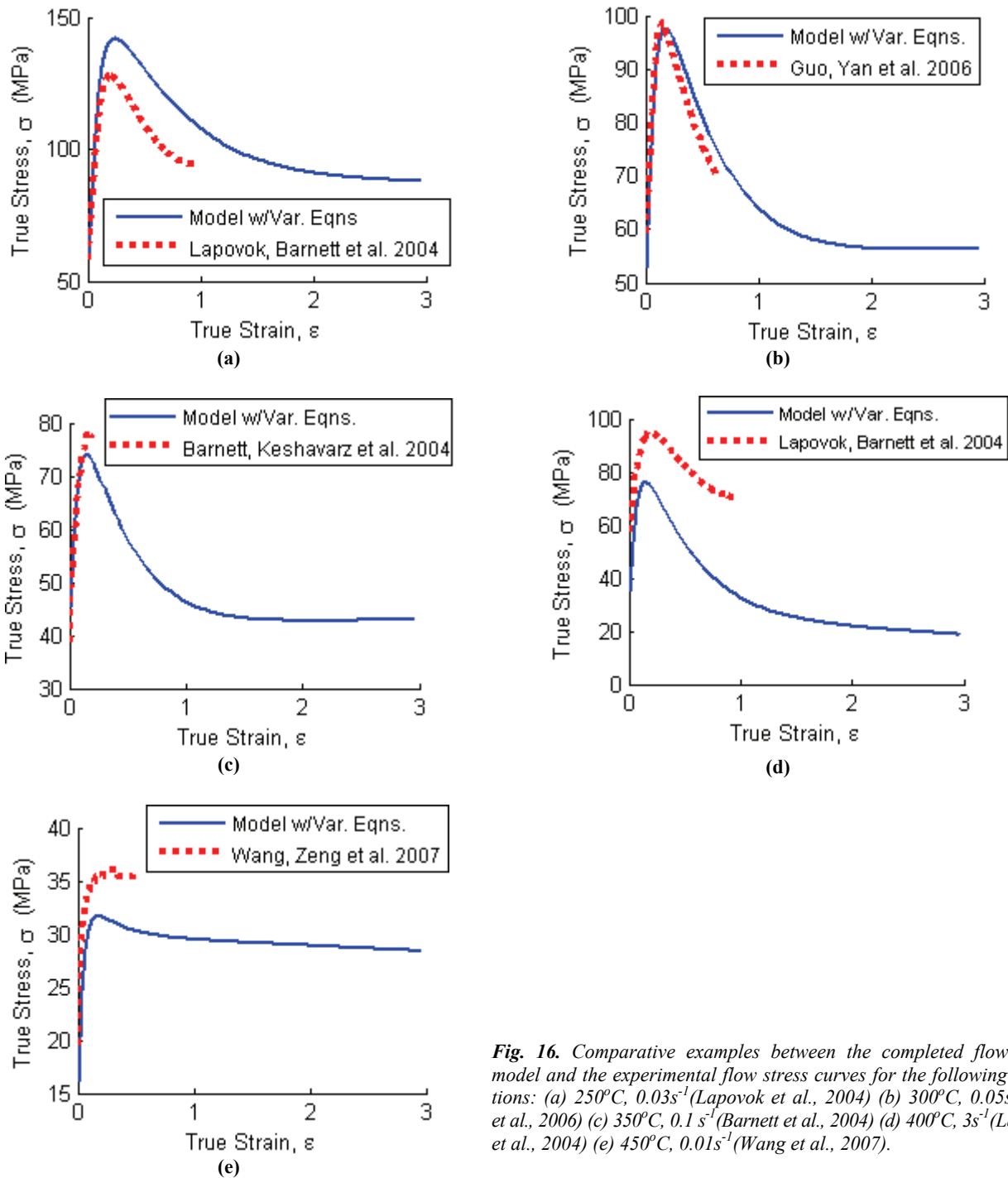experimental flow stress curves are presented in figure 16.

From figure 16 it can be seen that the variable equations of table 5 did not reproduce the experimental flow stress curves with reasonable accuracy. It is thought that due to the poor fit of some of the trend lines in figure 11 - figure 15 that the final equations derived for variables k, n, A, B, and C were skewing the flow stress results. In order to improve the accuracy of the flow stress model, the p and q values from the trends of figure 11 - figure 15 were changed slightly. The modified variable equations are presented in table 6 and provide an improved fit to the experimental curves as depicted in figure 17.

3.2. Numerical Simulation Analysis of Mg Extrusion

Initially, the numerical simulation of the 8 porthole die was performed with the experimental AZ31 flow stress found in literature. When creating the DEFORM$^{\text{TM}}$ 3-D material library entry for AZ31, only the hardening component of the AZ31 flow stress curves could be implemented and run successfully in DEFORM. When the softening component was added the extrapolation and interpolation coding within DEFORM was unable to determine the FEM

Table 5. *Variable equations as a function of strain rate and temperature.*

Hardening Variables	Softening Variables
$a = 1$ $\varepsilon_1 = 0.18$ $K = (6384.9e^{-6x10^{-3}T})\dot{\varepsilon}^{0.2796\ln T - 1.6531}$ $k = K/10$ $n = (3x10^{-5}T + 0.0039)\ln\dot{\varepsilon} + 1.6951e^{-3.2x10^{-3}T}$ $\xi = 1$ $\tau_{0t} = -0.08T + 59.832$ $m_I = -8x10^{-4}T + 0.6685$ $m_{II} = -6x10^{-5}T + 0.1174$ $m_{III} = 1.2x10^{-3}T - 0.4078$ $X_T = -4x10^{-4}T + 1.0193$	$A = (-1.1584T + 866.56)\dot{\varepsilon}^{1.2x10^{-3}T - 0.532}$ $B = (-1.5x10^{-3}T + 0.8042)\ln\dot{\varepsilon}$ $\quad + 0.3628e^{0.0027T}$ $C = 4x10^{18}T^{-5.9263}\dot{\varepsilon}^{0.4759\ln T - 2.6947}$ $D = -7.5x10^{-4}T + 0.9424$

When the variable functions from table 5 are combined with equation (7) and equation (8) the flow stress model is complete and is now a function of strain, strain rate, and temperature. Comparisons between the completed flow stress model and the

flow stress values for the simulation. The cause of this is having flow stress data from different sources

Fig. 16. *Comparative examples between the completed flow stress model and the experimental flow stress curves for the following conditions: (a) 250ºC, 0.03s⁻¹(Lapovok et al., 2004) (b) 300ºC, 0.05s⁻¹(Guo et al., 2006) (c) 350ºC, 0.1 s⁻¹(Barnett et al., 2004) (d) 400ºC, 3s⁻¹(Lapovok et al., 2004) (e) 450ºC, 0.01s⁻¹(Wang et al., 2007).*
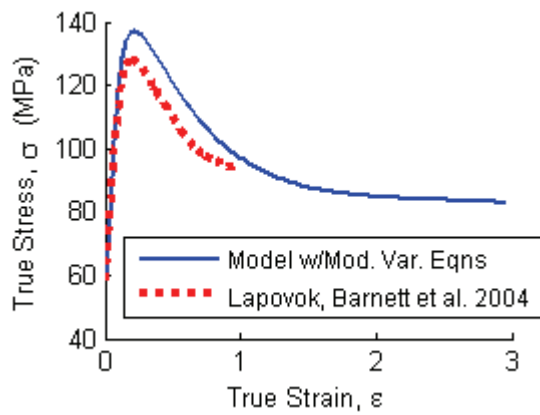
that have different negative slopes for the softening component of the flow stress curve and when the curves are extrapolated they intersect. The extrapolation and interpolation coding is then unable to calculate a flow stress value. If the softening and steady-state components were available with the experimental flow stress data this problem would most likely be averted. In addition to the flow stress data all the necessary material property information (e.g. thermal conductivity, Poisson ratio, etc.) that is required by DEFORM was also added to the AZ31

material library entry. Simulated results for the state variables from this effort are presented in figure 18. At the extrudate length shown in figure 18, the process is operating at steady-state conditions.
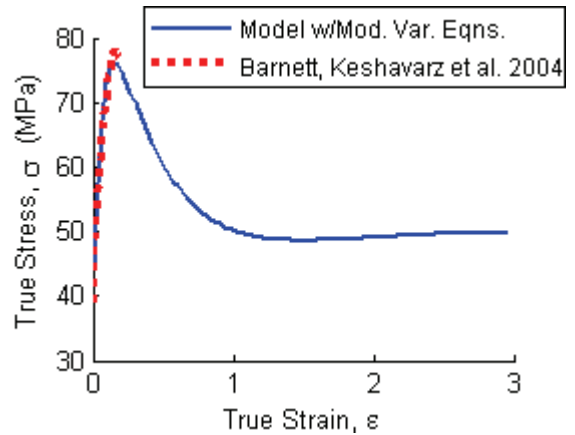
Table 6. *Modified variable equations as a function of strain rate and temperature.*
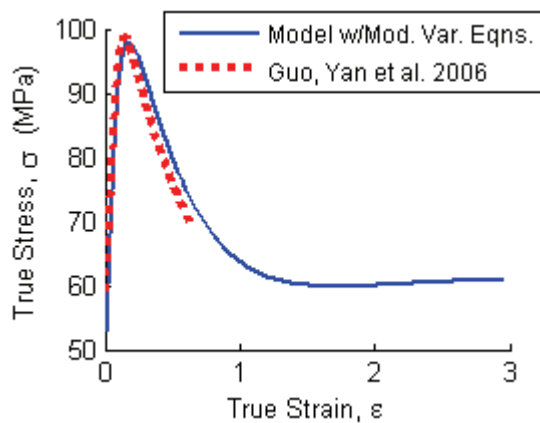
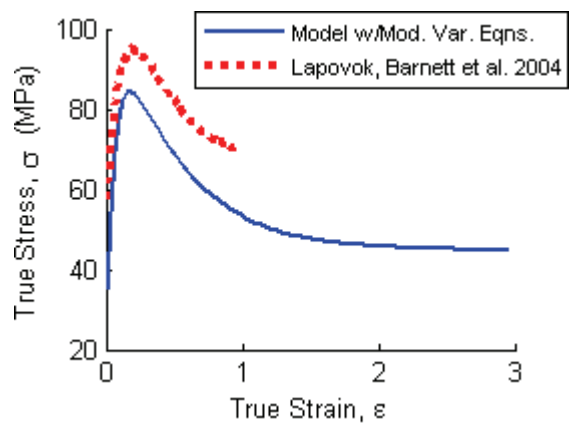| Hardening Variables	Softening Variables
$a = 1$	$A = (-1.157T + 865)\dot{\varepsilon}^{1.13x10^{-3}T - 0.533}$
$\varepsilon_1 = 0.18$	$B = (-1.5x10^{-3}T + 0.71)\ln\dot{\varepsilon}$
$K = (6384.9e^{-5.95x10^{-3}T})\dot{\varepsilon}^{0.276\ln T - 1.6525}$	$\quad + 0.3627e^{0.0027T}$
$k = K/10$	$C = 4x10^{18}T^{-5.916}\dot{\varepsilon}^{0.4741\ln T - 2.765}$
$n = (2.6x10^{-5}T + 0.0029)\ln\dot{\varepsilon} + 1.67e^{-3.05x10^{-3}T}$	$D = -7.2x10^{-4}T + 0.94$
$\xi = 1$	
$\tau_{0t} = -0.08T + 59.832$	
$m_i = -8x10^{-4}T + 0.6685$	
$m_{ii} = -6x10^{-5}T + 0.1174$	
$m_{iii} = 1.2x10^{-3}T - 0.4078$	
$X_T = -4x10^{-4}T + 1.0193$	

(a)

(c)

(b)

(d)

Fig. 17a-d. *Comparative examples between the flow stress model with modified variable equations of table 6 and experimental flow stress curves for the following conditions: (a) 250ºC, 0.03s⁻¹(Lapovok et al., 2004) (b) 300ºC, 0.05s⁻¹(Guo et al., 2006) (c) 350ºC, 0.1 s⁻¹(Barnett et al., 2004) (d) 400ºC, 3s⁻¹(Lapovok et al., 2004) (e) 450ºC, 0.01s⁻¹(Wang et al., 2007).*
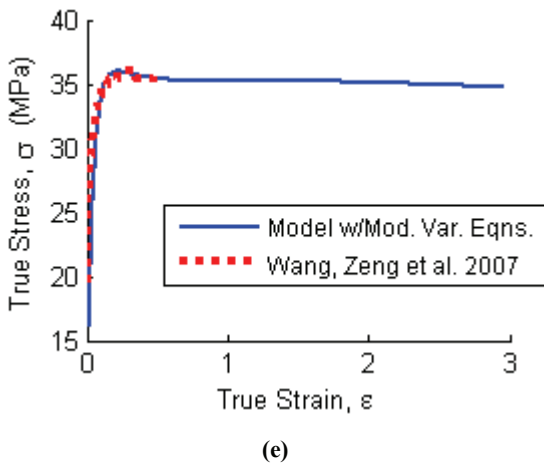
(e)

Fig. 17e. *Comparative examples between the flow stress model with modified variable equations of table 6 and experimental flow stress curves for the following conditions: (a) 250ºC, 0.03s⁻¹(Lapovok et al., 2004) (b) 300ºC, 0.05s⁻¹(Guo et al., 2006) (c) 350ºC, 0.1 s⁻¹(Barnett et al., 2004) (d) 400ºC, 3s⁻¹(Lapovok et al., 2004) (e) 450ºC, 0.01s⁻¹(Wang et al., 2007).*

Numerical simulation of the 8 port-hole die was then performed with the flow stress model. Equation (7), equation (8), and the equations from table 6 were programmed into a DEFORM subroutine (usr_mtr.f) and implemented into DEFORM™ 3-D. All the necessary material property information (e.g. thermal conductivity, Poisson ratio, etc.) was utilized from the previously created AZ31 material library entry. Simulated results for the state variables from this effort are presented in figure 19. At the extrudate length shown in figure 19, the process is operating at steady-state conditions.

In figure 19, the predicted flow stress distribution with the experimental AZ31 flow stress data is elevated in the port-hole die in comparison to the flow stress distribution predicted with the AZ31 flow stress model. The strain, strain rate, and temperature distribution for the flow stress model simulation were very similar to the experimental AZ31 flow stress data simulation.

(a)

(b)

(c)

(d)
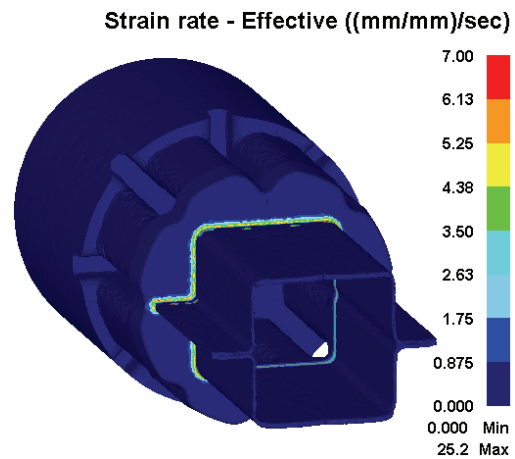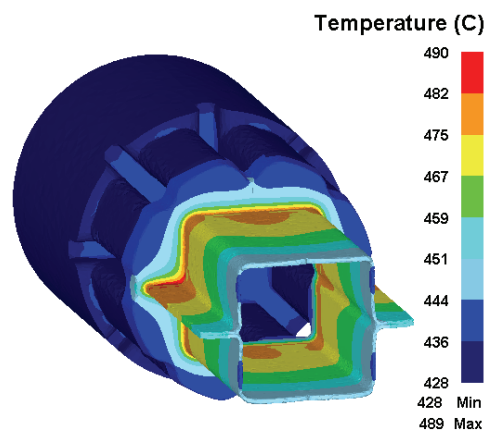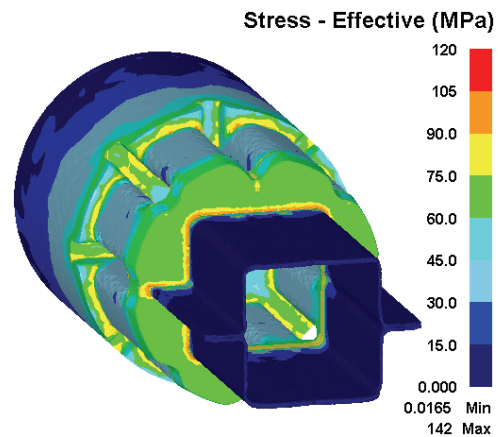
Fig. 18*. (a) Strain, (b) strain rate, (c) temperature, and (d) stress distributions during steady-state extrusion with experimental AZ31 flow stress data.*

(a)

(b)

Fig. 19. *DEFORM^{TM} 3-D simulated flow stress (a) with experimental AZ31 flow stress data and (b) with AZ31 flow stress model.*

4. DISCUSSION

4.1. Analysis of Modified Flow Stress Model

The comparison between the flow stress model curves, with the variable values from table 4, and the experimental flow stress curves show good agreement as depicted in figure 5. Several of the variable values and trends fro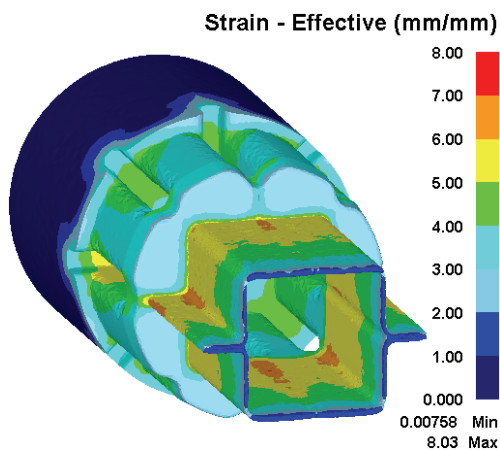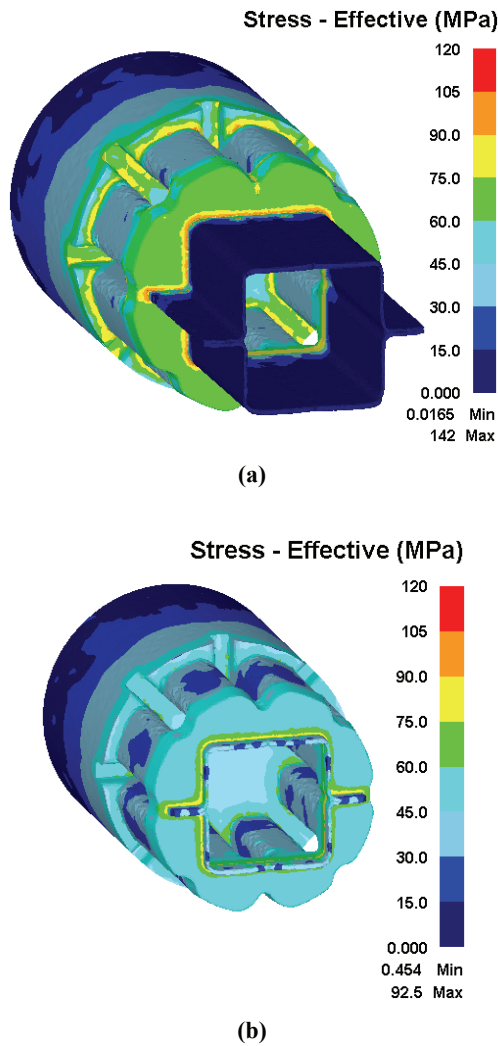m table 4 correlate well with experimental observations. For instance, variable *n* tends to increase with strain rate but decrease with the temperature within the ranges considered. Such behavior is similar to previously reported trends in literature for both AZ31 and AM30 (Jiang et al., 2006; Luo & Sachdev, 2007). Additionally, the fraction of grains undergoing twinning, X_T, ranges from 0.73-0.81. This aligns well with observations by Brown et al. (2005) that deformation twinning continues until approximately 80% of the microstructure is reoriented by a strain of 0.13 and continues at approximately that percentage for the duration of deformation. The beginning of this twinning fraction plateau at a strain of 0.13 (Brown et al., 2005) reasonably correlates to the value of 0.18 for ε_I in table 4, which is at the higher end of the range for ε_I (0.08-0.18) as specified by Barnett et al. (2005). Additionally, Jiang et al. (2007a) experimentally found that the volume fraction of twinning fell within the range of 60%-90% by a strain level of 0.06-0.12 for the majority of conditions tested, this correlates well with X_T and ε_I in table 4, respectively. The range for X_T in table 4 also decreases with increasing temperature as found for both AZ31 and AM30 by (Jain & Agnew, 2007; Jiang et al., 2007b).

The value for *a* (a = 1) in table 4 is lower than the range (*a*: 1.2-2) specified by Barnett et al. (2005) for their model, but it is only slightly outside this range. The trend for the twinning CRSS, τ_{0t}, from table 4 and figure 6c was found to decrease with increasing temperature. Since the model considers effective values for many of the variables, the variables essentially represent the average macroscopic behavior of a polycrystalline material at those specific temperature and strain rate conditions. Therefore, it is reasonable that τ_{0t} in this model would decrease with increasing temperature because it is well known that the initiation of twinning is more likely to occur and occur more easily at elevated temperatures. This results in the required flow stress to initiate deformation in volume I, σ_I to decrease as defined in equation (4). The decreasing behavior of the effective Schmid factor for only twinning, m_I with increasing temperature as represented in table 4 and figure 6d is believed to occur to offset some of the decreasing effect from τ_{0t} on σ_I. Similarly, the decreasing behavior of the effective Schmid factor for slip after twinning, m_{II} with increasing temperature (table 4 and figure 6e) occurs to offset the decreasing effect of *k* on σ_{II}. The increasing behavior of the effective Schmid factor for only slip, m_{III} with increasing temperature ((table 4 and figure 6f) is believed to occur to offset the increasing behavior of $(1 - X_T)$ on σ_{III} in the third term of equation (8).

The trends for the recovery variables *A*, *B*, *C*, and *D* behaved as expected. Variable *A* and *C* decreased with increasing temperature and decreasing strain rate (table 4 and figure 7) because the change between the ultimate stress, σ_{us} and the steady-state stress, σ_{ss} (figure 1) decreased with increasing temperature and decreasing strain rate. In other words as the peak in the flow stress curve decreases and approaches a profile similar to curve-A in figure 1 the

influence of variable *A* and *C* on the abrupt transitions of the flow curve can lessen. Additionally, *B*, which inversely controls the model's σ_{us}, increased with increasing temperature and decreasing strain rate (table 4 and figure 7) due to the fact that the σ_{us} decreases with increasing temperature and decreasing strain rate. Similar to variable *A* and *C*, variable *D* decreased with increasing temperature (table 4 and figure 7) because the steady-state stress, σ_{ss} (figure 1) decreases with increasing temperature.

With the variables from table 4, the flow stress model accurately predicted the hardening and softening components of the considered experimental curves. However, since the experimental curves only existed up to a small level of strain before failure in the compression test, the steady-state behavior of the predicted curves had to be assumed. The assumed portion of the predicted curves were constructed so that they continued along the same path or as closely as possible to the path that the end of the experimental curve was indicating and then leveled off to create the steady-state region.

The experimental curves generated from the compression tests failed at small levels of strain due to the shortcomings of the test. During the barreling of the compression sample, a hoop stress developed and eventually exceeded the tensile strength of AZ31, thus causing failure. If the compression sample was experiencing compression stresses from all sides, as it would during the extrusion process-thus diminishing premature failure, the flow stress curve would continue to the higher level of strains that are attainable in the extrusion process (figure 18a and figure 19a).

When the model variables were plotted with respect to strain rate and temperature (figure 6 and figure 7), three of the variables, *a*, ε_l, and ξ, were found to be constant through all strain rates and temperatures with values of $a = 1$, $\varepsilon_l = 0.18$, and $\xi = 1$. (It should be noted that with $\xi = 1$, the effect of the added curve-fitting hardening factor is minimized.) The remaining model variables of figure 6 and figure 7 either exhibited a variation with strain rate and temperature or just a variation with temperature. The variables that exhibited a variation with strain rate and temperature (*k, n, A, B, and C*) behaved with either a logarithmic tend $\left(r\ln(\dot{\varepsilon}) + s \right)$ or the power-law trend $\left(r\dot{\varepsilon}^{\,s} \right)$. Variables *A*, *B*, and *C* closely matched one of these trends as portrayed in figure 9 and figure 10 for the majority of the temperatures as a function of strain rate. There was de-

viation from the trends for both variables *A* and *B* for the 450°C case. This may be a result of experimental scatter in the data points; however, more experimental data sets are needed to confirm this. Variables *k* and *n* also closely matched one of these trends, as portrayed in figure 8, but only for the set of experimental data for each temperature with the most data points. For instance, there are two data sets making up the *k* and *n* curves for the 450°C case. One set has a *k* and *n* variable value for each strain rate considered (Wang et al., 2007) but the second set only has a single *k* and *n* variable value for the strain rate of 0.1 s^{-1} (Barnett et al., 2004). This single variable value is the lower value in both variable curves at a strain rate of 0.1 s^{-1} and does not trend as well as with the other values from the other set. This is similar for the 400°C case, where data set one has a *k* and *n* variable value for the strain rates 0.03, 0.3, and 3s^{-1} (Lapovok et al., 2004) but the second set has a single *k* and *n* variable value for the strain rate 0.1 s^{-1} (Barnett et al., 2004). This single *k* and *n* variable value also does not trend as well as with the values from the other set. It is believed that initial material conditions such as grain size or texture are causing this inconsistency in the trends for both the *k* and *n* curves. However, initial grain diameter and/or other consistent initial material condition information were not reported in all the experimental data sets that came from literature. Subsequently, trying to account for the trending inconsistency through the initial grain diameter and/or other consistent initial material condition was not possible at this time. Nevertheless, a general comparison can be made about the possible influences of texture. According to figure 6 of Takuda et al., (2005) the strain-hardening exponent, *n* increases with a decreasing rate with respect to strain rate on a log-plot as opposed to increasing with a constant rate with respect to strain rate on a log-plot as shown by the several data sets considered in figure 8b. In the study conducted by Takuda et al. (2005) the material of interest was AZ31 3.0mm rolled sheet. The AZ31 rolled sheet of Takuda et al. (2005) would be expected to have a strong texture. The material considered in the several data sets of figure 8b is in the as-cast homogenized condition with a random crystal orientation. Therefore, the strong texture of the AZ31 rolled sheet may be the cause of the discrepancy in the strain-hardening exponent behavior. Although, new experimental data sets conducted at varying initial material conditions would have to be

performed to verify and account for such a trending inconsistency.

The *r* and *s* values from the logarithmic and power-law tend lines of figure 8, figure 9, and figure 10 were found as functions of temperature by plotting with respect to absolute temperature as presented in figure 11 - figure 15. The trend lines added to these plots were either of the linear form $(pT + q)$, logarithmic form $(p \ln(T) + q)$, exponential form (pe^q) or the power-law form (pT^q). The trend lines of figure 11 - figure 15 with a coefficient of determination, R^2 value greater than or equal 0.80 was only 50%. Consequently, future outcomes for *k, n, A, B,* and *C* will be skewed by these *r* and *s* relationships. This was confirmed in figure 16 by the low agreement between the flow stress model, with the variable functions of table 5, and the experimental flow stress curves. In figure 16, the flow stress model with the variable functions of table 5 tends to over predict the experimental flow stress curves at lower temperatures and under predict at the higher temperatures.

As mentioned earlier, it is believed that initial material conditions are causing this inconsistency in the trends for the *r* and *s* values of figure 11 - figure 15. However, new experimental data sets conducted at varying initial material conditions would have to be performed to verify and account for such a trending inconsistency.

The remaining variables, τ_{0t}, m_i, m_{ii}, m_{iii}, X_t, and *D*, were found to be only a function of temperature (table 5) with each variable function having a coefficient of determination, R^2 value of 1. Consequently, future outcomes for the variables τ_{0t}, m_i, m_{ii}, m_{iii}, X_t, and *D* are likely to be predicted accurately by their corresponding function.

In order to improve the accuracy of the flow stress model, the *p* and *q* values from the trends of figure 11 - figure 15 were changed slightly. The modified set of variable equations is presented in table 6 and provides an improved fit to the experimental curves as depicted in figure 17. The small adjustments in several of the equations seem to have minimized the over prediction of the experimental flow stress curves at lower temperatures and under prediction at the higher temperatures. There is still some disagreement between the model and the experimental curves for figure 17a and d, but as previously mentioned this could be a result of an initial material condition. A drawback in making the small adjustments to the original equations of table 5 to produce the equations of table 6 is that the influence of the initial material condition is being minimized or in effect being ignored. For a robust and accurate flow stress model the initial material condition must be accounted for along with a wide range of temperature and strain rate conditions.

4.2. Numerical Simulation Analysis of Mg Extrusion

Implementing experimental flow stress curves and material data into DEFORM is the typical process performed by industrial and research community users of the software when a library entry does not exist for the material of interest. Therefore, by performing a numerical simulation of the 8 port-hole die with experimental flow stress first, which would normally be the benchmark, a set of results was produced that were used to compare to the numerical simulations of the 8 port-hole die with the flow stress model.

It should be noted that if the experimental flow stress is too narrow in its range for strain, strain rate, and/or temperature when implemented into DEFORM, the extrapolation coding within DEFORM is activated often, and consequently, the accuracy of the simulated results may be negatively affected. However, for this study a sufficient amount of AZ31 as-cast homogenized flow stress data was found.

In order to keep the model bounded in DEFORM, constrictions had to be added to a few variables, as shown in table 7. Most of these constraints are used at the onset of the simulation when the strain rate has a zero value and causes the model to become unbounded. Due to these constraints, further empirical and/or theoretical development is needed for the flow stress model.

Table 7. Variable constraints for model variables.

$n > 0$	$A > 0$
$\tau_{0t} > 0$	$B > 0$
$0 < m_I \leq 0.5$	$C > 0$
$0 < m_{II} \leq 0.5$	
$0 < m_{III} \leq 0.5$	

In figure 18 are the DEFORM™ 3-D results for the hollow AZ31 structural component while using the experimental AZ31 flow stress data. The results shown for strain, strain rate, and temperature are

behaving as expected. However, in figure 19, the experimental flow stress distribution is shown again and compared directly to the flow stress distribution predicted by the model. It is clear that the predicted flow stress distribution with the experimental data is elevated in the port-hole die in comparison to the flow stress distribution predicted with the flow stress model. The cause for this is the lack of the material softening component in the experimental data that was implemented into DEFORM. As described earlier, when creating the DEFORM™ 3-D material library entry for AZ31, only the hardening component of the AZ31 flow stress curves could be implemented and run successfully in DEFORM. However, since the flow stress model can account for the softening component, the predicted results for the flow stress distribution is lower, which was expected. If a comparison is made between the stress distributions without considering the magnitude of the stress, the actual spreading of the stress distribution is similar in both simulations. Therefore, suggesting the model does perform correctly in the DEFORM™ 3-D software package because it performs similar to the benchmark simulation.

The benefit of using a flow stress model over the experimental data is that once the initial material condition is accounted for in the model, the initial material condition will be able to be entered into DEFORM as a "initial material condition" field entry at the beginning of the simulation. This will increase the accuracy of the flow stress prediction for the actual AZ31 material being considered. Conversely, when experimental flow stress data is used to calculate flow stress, the experimental data will generally have an initial material condition that is different from the actual material being considered, thus, producing simulated results that are not as accurate. In order to correct for this a new AZ31 material library entry needs to be entered with new flow stress data generated from the actual material of interest - a process that would be an inefficient use of resources. As a consequence, it is believed that using the flow stress model that eventually accounts for the initial material condition makes the simulation of the extrusion process more accurate and efficient.

In terms of processing, the regions behind the port-hole die ribs, which support the plug, (figure 18) were found to require a high strain and stress response from the billet. Rounding the rib edges will streamline the billet flow and lower the required strain and stress response. This will potentially minimize extrudate defects and improve quality.

5. CONCLUSIONS

In this study, a new empirical flow stress model has been developed for as-cast homogenized AZ31 compression test flow stress data. It produces reasonably accurate results for the temperature range: 250-450°C and strain rate range: 0.001-20 s^{-1} and is capable of predicting the hardening, softening, and steady-state components of the flow stress curve as only a function of strain, strain rate, and temperature.

Moreover, the following conclusions can be made from this modeling effort:
- A simple set of algebraic equations for the flow stress that are based on the Sachs assumption and an empirical account of crystallographic slip and deformation twinning were developed.
- Using an effective Schmid factor to quantify the effect of different portions of the polycrystalline sample as opposed to using the specific Schmid factor for each crystal and then relating them back to each other with iterative polycrystalline equations as required by the scientific (or self-consistent) models, simplifies the required mathematics significantly.
- Implementation of the flow stress model into the industry-accepted software package, DEFORM™ 3-D, and numerically simulating an AZ31 automobile structural component fabricated with a porthole die was successfully accomplished.
- For a robust and more accurate flow stress model the initial material condition must be accounted for along with a wide range of strain, strain rate, and temperature conditions.
- Once the initial material condition is accounted for in the flow stress model it will more accurately and efficiently predict the flow stress response for the actual material being considered than with a generic experimental flow stress based material library entry in DEFORM™ 3-D.

Empirical and theoretical development is not yet complete for the flow stress model but to date the results are reasonably accurate.

ACKNOWLEDGEMENTS

REFERENCES

Agnew, S. R., Duygulu, Ö., 2005, Plastic anisotropy and the role of non-basal slip in magnesium alloy AZ31B, *International Journal of Plasticity*, 21(6), 1161-1193.

Barnett, M., Keshavarz, Z., Ma, X., 2006, A semianalytical Sachs model for the flow stress of a magnesium alloy, *Metallurgical and Materials Transactions A*, 37(7), 2283-2293.

Barnett, M. R., 2001, Influence of deformation conditions and texture on the high temperature flow stress of magnesium AZ31, *Journal of Light Metals*, 1(3), 167-177.

Barnett, M. R., 2005, Texture, twinning and uniform elongation of wrought magnesium, *Materials Science Forum*, 495-497, 1079-1084.

Barnett, M. R., 2007a, Twinning and the ductility of magnesium alloys: Part I: "Tension" twins, *Materials Science and Engineering: A*, 464(1-2), 1-7.

Barnett, M. R., 2007b, Twinning and the ductility of magnesium alloys: Part II. "Contraction" twins, *Materials Science and Engineering: A*, 464(1-2), 8-16.

Barnett, M. R., Davies, C. H. J., Ma, X., 2005, An analytical constitutive law for twinning dominated flow in magnesium, *Scripta Materialia*, 52(7), 627-632.

Barnett, M. R., Keshavarz, Z., Beer, A. G., Atwell, D., 2004, Influence of grain size on the compressive deformation of wrought Mg-3Al-1Zn, *Acta Materialia*, 52(17), 5093-5103.

Beer, A. G., Barnett, M. R., 2007, Microstructural Development during Hot Working of Mg-3Al-1Zn, *Metallurgical and Materials Transactions A*, 38(8), 1856-1867.

Brown, D. W., Agnew, S. R., Bourke, M. A. M., Holden, T. M., Vogel, S. C., Tomé, C. N., 2005, Internal strain and texture evolution during deformation twinning in magnesium, *Materials Science and Engineering: A*, 399(1-2), 1-12.

Francillette, H., Gavrus, A., Lebensohn, R. A., 2003, A constitutive law for the mechanical behavior of Zr 702, *Journal of Materials Processing Technology*, 142(1), 43-51.

Gronostajski, Z., 2000, The constitutive equations for FEM analysis, *Journal of Materials Processing Technology*, 106(1-3), 40-44.

Guo, Q., Yan, H. G., Chen, Z. H., Zhang, H., 2006, Elevated temperature compression behaviour of MgAlZn alloys, *Materials Science and Technology*, 22, 725-729.

Hosford, W. F., 1993, *The Mechanics of Crystals and Textured Polycrystals*, Oxford University Press, New York.

Jain, A., Agnew, S. R., 2007, Modeling the temperature dependent effect of twinning on the behavior of magnesium alloy AZ31B sheet, *Materials Science and Engineering: A*, 462(1-2), 29-36.

Jiang, L., Jonas, J. J., Luo, A. A., Sachdev, A. K., Godet, S., 2006, Twinning-induced softening in polycrystalline AM30 Mg alloy at moderate temperatures, *Scripta Materialia*, 54(5), 771-775.

Jiang, L., Jonas, J. J., Luo, A. A., Sachdev, A. K., Godet, S., 2007a, Influence of {10-12} extension twinning on the flow behavior of AZ31 Mg alloy, *Materials Science and Engineering: A*, 445-446, 302-309.

Jiang, L., Jonas, J. J., Mishra, R. K., Luo, A. A., Sachdev, A. K., Godet, S., 2007b, Twinning and texture development in two Mg alloys subjected to loading along three different strain paths, *Acta Materialia*, 55(11), 3899-3910.

Lapovok, R. Y., Barnett, M. R., Davies, C. H. J., 2004, Construction of extrusion limit diagram for AZ31 magnesium alloy by FE simulation, *Journal of Materials Processing Technology*, 146(3), 408-414.

Lebensohn, R. A., Tome, C. N., 1993, Self-consistent anisotropic approach for the simulation of plastic deformation and texture development of polycrystals: application to zirconium alloys, *Acta Metallurgica et Materialia*, 41(9), 2611-2624.

Levesque, J., Inal, K., Neale, K. W., Mishra, R. K., Luo, A. A. 2006, Numerical modelling of large strain deformation in magnesium, San Antonio, TX, United States, 239-243.

Levesque, J., Inal, K., Neale, K. W., Mishra, R. K., Luo, A. A., Jiang, L., 2007, Numerical modelling of large strain deformation in magnesium alloy AM30, Orlando, FL, United States, 11-16.

Li, L., Zhou, J., Duszczyk, J., 2006, Determination of a constitutive relationship for AZ31B magnesium alloy and validation through comparison between simulated and real extrusion, *Journal of Materials Processing Technology*, 172(3), 372-380.

Luo, A. A., Sachdev, A. K., 2007, Development of a new wrought magnesium-aluminum-manganese alloy AM30, *Metallurgical and Materials Transactions A: Physical Metallurgy and Materials Science*, 38(6), 1184-1192.

Mathis, K., Trojanova, Z., Lukac, P., 2002, Hardening and softening in deformed magnesium alloys, *Materials Science and Engineering A*, 324(1-2), 141-144.

Mathis, K., Trojanova, Z., Lukac, P., Caceres, C. H., Lendvai, J., 2004, Modeling of hardening and softening processes in Mg alloys, *Journal of Alloys and Compounds*, 378(1-2), 176-179.

Meyers, M. A., Vohringer, O., Lubarda, V. A., 2001, The onset of twinning in metals: a constitutive description, *Acta Materialia*, 49(19), 4025-4039.

Remy, L., 1978, Kinetics of FCC Deformation Twinning and Its Relationship to Stress-Strain Behaviour, *Acta Materialia*, 26, 443-451.

Schindler, I., Kliber, J., Boruta, J.,1996, Plastometric and computer modeling of deformation behavior of Nb-bearing HSLA-steel, *Metalurgija*, 35(4), 211-214.

Sheng, Z. Q., Shivpuri, R., 2006, Modeling flow stress of magnesium alloys at elevated temperature, *Materials Science and Engineering: A*, 419(1-2), 202-208.

Slooff, F. A., Zhou, J., Duszczyk, J., Katgerman, L., 2007, Constitutive Behavior of Wrought Magnesium Alloy AZ61, *Magnesium Technology 2007* Orlando, FL; USA, 363-368.

Srivatsan, T. S., Wei, L., Chang, C. F., 1995, The tensile behaviour of rapidly solidified magnesium alloys, *Journal of Materials Science*, 30(7), 1832-1838.

Staroselsky, A., Anand, L., 1998, Inelastic deformation of polycrystalline face centered cubic materials by slip and twinning, *Journal of the Mechanics and Physics of Solids*, 46(4), 671-696.

Staroselsky, A., Anand, L., 2003, A constitutive model for hcp materials deforming by slip and twinning: application to magnesium alloy AZ31B, *International Journal of Plasticity*, 19(10), 1843-1864.

Tadano, Y., Kuroda, M., Noguchi, H., Shizawa, K., 2007, A polycrystalline analysis of hexagonal metal based on the homogenized method, *Key Engineering Materials*, 340-341 II, 1049-1054.

Takuda, H., Morishita, T., Kinoshita, T., Shirakawa, N., 2005, Modelling of formula for flow stress of a magnesium alloy AZ31 sheet at elevated temperatures, *Journal of Materials Processing Technology*, 164-165, 1258-1262.

Van Houtte, P., 2001, Fast calculation of average Taylor factors and Mandel spins for all possible strain modes, *International Journal of Plasticity*, 17(6), 807-818.

von Mises, R., 1928, Mechanik der plastischen Formänderung von Kristallen." *Z. Angew. Math. Mech.*, 8, 161-185.

Wang, Y., Zeng, X., Ding, W., Luo, A. A., Sachdev, A. K., 2007, Development and Validation of Extrusion Limit Diagram for AZ31 and AM30 Magnesium Alloys, *Materials Science Forum*, 546-549, 327-332.

Wonsiewicz, B. C., Backofen, W. A., 1967, Plasticity of Magnesium Crystals, *AIME Met. Soc. Trans.*, 239(9), 1422-1431.

NUMERYCZNE MODELOWANIE NAPREZENIA ODKSZTALCAJACEGO W PRZYPADKU DUZYCH ODKSZTALCEN W STOPIE MAGNEZU AZ 31

Streszczenie

Isniejacy model naprezenia uplastyczniajacego zaproponowany przez Barnetta zostal przeanalizowany uzywajac danych z literatury dla odlanego i homogenizowanego stopu AZ31 poddanego probom sciskania w zakresie temperatur od 250 do 450 $^{\circ}$C i predkosci odksztalcenia od 0.001 do 20 s^{-1}. Analize te przeprowadzono w celu zwerifikowania czy model ten nadaje sie do zastosowania do procesu wyciskania wspolbiezniego stopu AZ31. Model ten sprawdzil sie w przewidywaniu krzywej umocnienia lecz nie byl w stanie przewidziec znaczacego zmiekczenia materialu typowego dla odlanego i homogenizowanego stopu magnezu tuz przed peknieciem. W celu poprawienia tego limitujacego faktu opracowano poprawke dla tego zakresu temperatur i predkosci odksztalcenia. Ten zmodyfikowany model naprezenia uplastyczniajacego zostal nastepnie zastosowany w programie elementow skonczonych DEFORM^{TM} 3-D w celu analizy wyciskania wspolbieznego na goraco przez matryce mostkowa profilu ze stopu AZ31.